

Research Article

Development of an Anchoring System for the Soft Asteroid Landing Exploration

Zhijun Zhao ¹, Shuang Wang,^{2,3} Delun Li,¹ Hongtao Wang,¹ Yongbing Wang,⁴
and Jingdong Zhao ⁵

¹Beijing Key Laboratory of Intelligent Space Robotic Systems Technology and Applications, Beijing Institute of Spacecraft System Engineering, Beijing 100092, China

²Research Center of Satellite Technology, Harbin Institute of Technology, Harbin 150080, China

³Space Star Technology Co., LTD., 100086, China

⁴Beijing Institute of Mechanics and Electricity, Beijing 100092, China

⁵State Key Laboratory of Robotics and System, Harbin Institute of Technology, Harbin 150080, China

Correspondence should be addressed to Zhijun Zhao; zhaozhj@yahoo.com

Received 17 January 2018; Accepted 30 October 2018; Published 7 February 2019

Academic Editor: Christopher J. Damaren

Copyright © 2019 Zhijun Zhao et al. This is an open access article distributed under the Creative Commons Attribution License, which permits unrestricted use, distribution, and reproduction in any medium, provided the original work is properly cited.

The landing mechanism is easy to flow away from the surface of the asteroid, as there is nearly no gravity on the asteroid. One of the most problems for the asteroid landing exploration is to anchor the landing mechanism on the asteroid surface. In the paper, an anchoring system employed on the soft asteroid anchoring is designed. It is mainly composed of penetrating unit, advancing unit, winding unit, damping unit, and so on. On the basis of the mechanical design, the resistance characteristic of the anchor body in penetrating process is analyzed, and the shape of the anchor tip is designed with the least resistance as the constraint. Then, the validity of the anchor tip design is tested by comparing penetrating ability of different anchor tips. Finally, the penetrating and the anchoring performances of the anchoring system are tested in a variety of media.

1. Introduction

Asteroid is rich in minerals and contains information of the solar system forming and evolving. It has high scientific and economic value [1, 2]. Through the exploration of asteroid, we can understand the asteroid more and find out clues of the formation of the planetary system and its evolution history. We can find the answers on the origin of the solar system and the life and explore and use asteroid resources. Moreover, asteroid exploring can promote the progress of deep space exploration technology and lay the foundation for opening up a new space [3]. Asteroid exploring methods mainly include ground observation, orbital detection [4], sample returning [5–7], and landing exploration [8–10]. However, landing exploration is a comprehensive and effective way to understand the characteristics of the asteroid. Currently, the landing exploration on the Moon and the Mars has been realized.

Asteroid surface shows microgravity. One of the difficulties of asteroid landing exploration is that the landing mechanism on its surface can easily rebound or drift away which is different from the traditional large landing mechanism (the Moon, Mars, and other landing mechanism). All the exploration of the asteroid landing mechanism must be carried out after its stable anchoring on the asteroid surface. Therefore, the anchoring system is the key that affects the success of asteroid landing detection. Rosetta's Philae Lander is designed with an anchoring system [11].

There are a large number of asteroids, and the media characteristics of different asteroids vary widely. Soft surface asteroid is easy to realize anchoring. In this paper, an anchoring system will be developed for the C class and other soft asteroids. The anchoring system developed in the paper is different from the Philae's on the structural design, and the main differences are as follows: the penetrating unit of this anchoring system is deformable actively, and the claws and

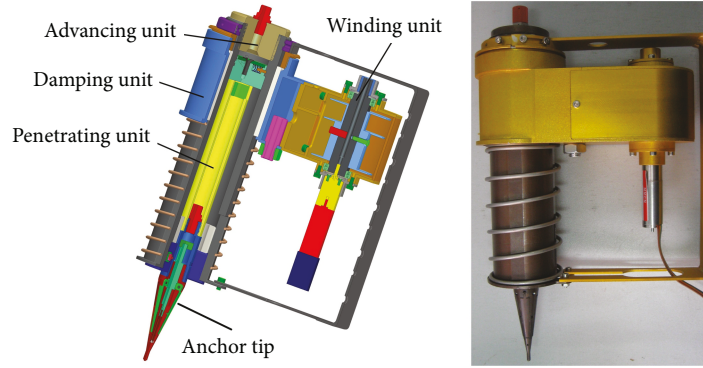


FIGURE 1: Schematic diagram and picture of the anchoring system.

TABLE 1: Performance parameters of the anchoring system.

Categories	Parameters
Mass	1.5 kg
Volume	$260 \times 175 \times 65$ mm
Penetrating speed	20~100 m/s
Rope length	2 m
Winding speed	0.2 m/s
Winding force	20 N
Anchoring time	≤ 10 s
Anchoring force	≥ 50 N

barbs can deploy after penetrating but they are hidden on the anchor tip before penetrating. Thus, the penetrating resistance is less than the passive deformable barbs in the Philae anchoring system. In this way, the penetrating depth can be larger. Furthermore, actively deployed barbs can generate irregular and plastic interaction with the asteroid media, which can enhance the anchoring force compared with the passive barbs. The main study target of the paper is the asteroid anchoring system, containing mechanical design, penetration resistance, and shape design of the anchor tip. By the way, the performance of the anchoring system is tested in a variety of media.

2. Anchoring System Design

The asteroid landing mechanism establishes a mechanical connection between the anchoring system and the asteroid surface, thereby anchoring the landing mechanism on the asteroid surface. Media characteristics of the asteroid must be considered in designing an anchoring system. According to the advantages and disadvantages of various anchoring methods proposed by Steltzner and Nasif [12], and based on the strong adaptability of anchoring system to media, this paper introduces the “chain mode” to design the anchoring system. The anchoring system consists of penetrating unit, advancing unit, winding unit, damping unit, and so on. Its schematic diagram and the photograph are shown in Figure 1. The performance parameters are shown in Table 1. The installing location of the anchoring system on the landing mechanism is shown in Figure 2 [13].

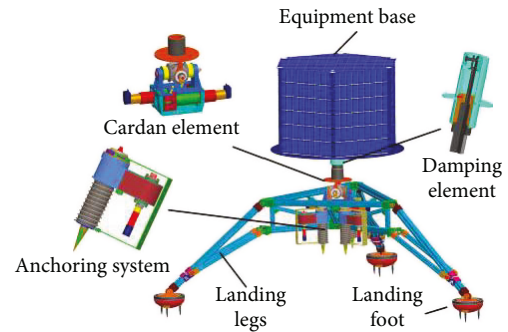


FIGURE 2: Installing location of the anchoring system on the landing mechanism.

The advancing unit is ignited when the central control system receives the landing signals, and the penetrating unit pushed out the advancing unit at the high speed, and then the penetrating unit is penetrated into the asteroid. At the end of the penetration, the ignition inside the penetrating unit is triggered, inducing the deformation of the anchoring tip. The winding unit rewinds the rope while penetrating unit is fired. When the rope is tensioned at the end of the anchoring, the spring in damping unit can be compressed to protect the motor and reducer.

2.1. Penetrating Unit. In the paper, an active deformation penetrating unit is designed, and its mechanical structure is shown in Figure 3. The penetrating unit mainly contains anchor tip, anchor claw, barb, handspike, piston, pyrotechnics, anchor body, and so on. The shape and size design of the anchor tip will be analyzed in Section 3. As penetrating unit gets onto the asteroid surface, the control system ignites the pyrotechnics and generates high-pressure gas. The gas pushes the handspike via the piston, which induces the splay of the claw and the barbs. The deployed penetrating unit is shown in Figure 4. In soft media, the claws and barbs are fully opened, and the open barbs increase the contact area between the anchor tip and the media, increasing the anchoring force. In hard media, the claws and barbs will lead to irregular and plastic deformation when opening due to the great thrust generated by the pyrotechnics. This phenomenon is similar to the effect of expansion bolt, which can increase the anchoring force.

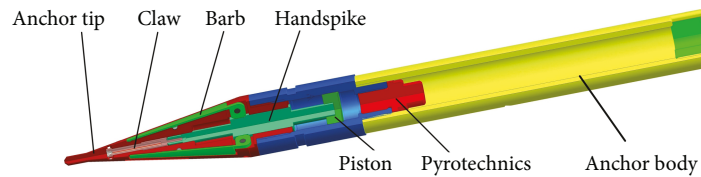


FIGURE 3: Schematic diagram of the penetrating unit.



FIGURE 4: Schematic diagram of the penetrating unit after splaying.

2.2. Advancing Unit. Mechanical structure of the advancing unit is shown in Figure 5. It mainly contains the pyrotechnics, combustion chamber, telescoping pin, piston, expansion cylinder, damping pad, flange, limiting pin, and so on. The high-pressure gas generated as the pyrotechnics pushes the piston moving quickly in the expansion cylinder. The quick moving piston will cause the penetrating unit to reach a high speed. When the piston moves to the bottom of the expansion cylinder, it is prevented by the damping pad, and the penetrating unit flies out of the advancing unit at a high speed.

A number of telescoping pins are distributed in the radial direction of the piston, and the telescoping of the pins is generated by the compression spring. There are three roles of the telescoping pins. Firstly, it can make the piston stay in the top of the expansion cylinder before the ignition of pyrotechnics. Secondly, the telescoping pins can be compressed when the gas pressure reaches a certain value, which makes the powder of the pyrotechnics burn sufficiently. Thirdly, the gas pressure on the piston can be adjusted by adjusting the number of telescoping pins, so ultimately different penetrating speed of the penetrating unit can be obtained. The stopping pin is similar to the telescoping pin that can be retracted inside the flange, which brings the mechanical limit to the penetrating unit and prevents it from falling off from the advancing unit.

2.3. Winding Unit. The winding unit is used to tense the cord attached to the tail of the penetration unit, so that the landing mechanism can cling to the asteroid surface. The mechanical structure of the winding unit is shown in Figure 6. It mainly includes brake, motor, reducer, reel, winding shaft, shell, and cord tank. The cord attaching to the penetrating unit end is stored inside the storage chamber 1, which is connected to the winding shaft before being fired, and the cord is connected to the control system via the storage 2 after the winding shaft. In order to prevent the cord connected to the control system from breaking when the winding shaft is wound, the cord is also stored in the storage 2. The diameter of the reel corresponding to the storage 2 is smaller than that of the storage 1, which can reduce the length of the cord in storage 2.

When the penetrating unit is fired, one part of the cord inside the storage 1 is pulled out by the penetrating unit for establishing a mechanical connection between the asteroid and the landing mechanism, and the other part in storage 1 is wound around the winding shaft. When the cord stored in the storage 1 is fully pulled out, the cord between the end of the penetrating unit and the winding shaft is tensioned. After proper adjustment, the motor is powered off and the brake is locked, so the anchoring of the landing mechanism is realized.

2.4. Damping Unit. The mechanical structure of the damping unit is shown in Figure 7. It mainly contains sliding tube, sleeve, spring, etc. The damping unit is mounted on the expansion cylinder of the advancing unit via a sliding tube which can slide on the outer wall of the expansion cylinder. The damping unit has two functions. Firstly, the winding unit will generate an impact load momentarily at the end of the winding. On this impact load, the sleeve drives the sliding tube to slide along the outer wall of the expansion cylinder and compress the spring, so that the motor and the reducer are protected from the impact load. Secondly, after the anchoring system has anchored some time, the cord between the penetrating unit and the winding unit may become loosened due to external factors, so the connection between the landing mechanism and the asteroid will become loose. It will induce slight floating of the landing mechanism on the surface of the asteroid, which will make the landing mechanism not stable enough to support the normal operation of the instruments. The compressed spring has an upward thrust on the sleeve, and when the cord is loosened, the sleeve will slide upwards under the action of the spring so that the loose cord is tensioned. The spring keeps the cord in tensioned state every time.

3. Shape of the Anchor Tip

There is antforce on the anchor body when penetrating, which affects its penetrating depth. The deeper the anchor body is, the larger the anchoring force becomes. Thus, it is significant to discuss the relationship between the initial condition of the anchor body and its penetrating depth, which is helpful to the design of the anchoring system.

The anchor body of the anchoring system forms cavity along the penetrating track, and the radial stress on the surface of the cavity can be used to describe the normal stress on the surface of the anchor body during penetration. The spherical cavity expansion model considers that a ball-symmetric cavity is formed when penetrating and the cavity expands outward from a radius of zero at a velocity

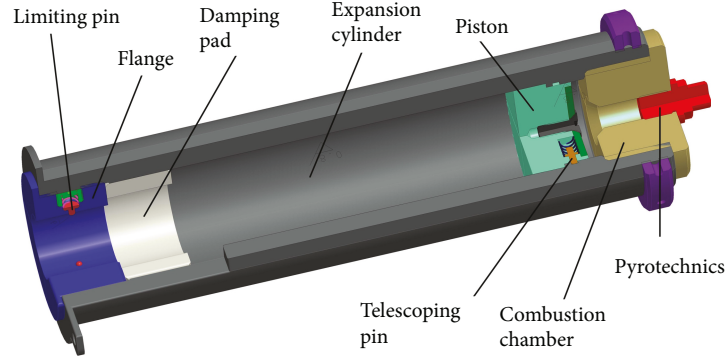


FIGURE 5: Schematic diagram of the advancing unit.

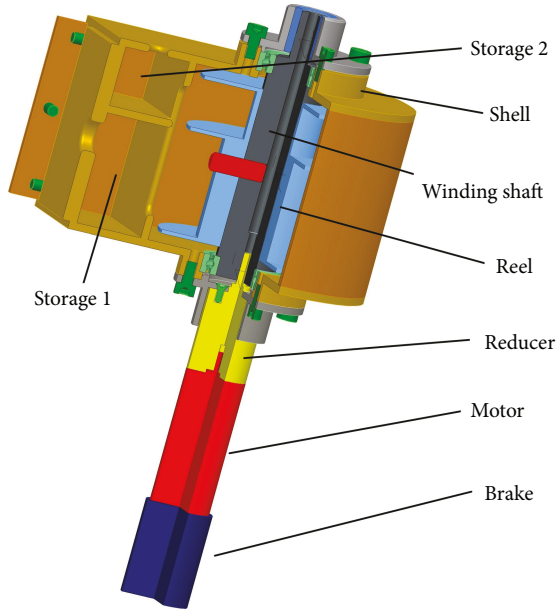


FIGURE 6: Schematic diagram of the winding unit.

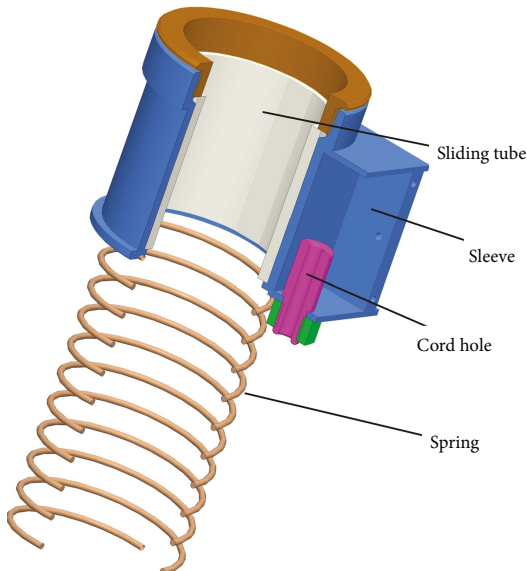


FIGURE 7: Schematic diagram of the damping unit.

V , and then forms a plastic response zone and an elastic response zone as shown in Figure 8. The plastic response zone has the radius $r = Vt$ and $r = ct$ for the boundary (where c is the elastic-plastic interface velocity, and t is the time).

The constitutive equation of the plastic response zone is based on the Mohr-Coulomb yield criterion. The state equation is described by the lock hydrostatic pressure (pressure-volume strain) model, and the elastic response zone is incompressible elastic material [14–16]. The penetrating process is analyzed as follows.

When anchor body penetrating, based on the cavity expansion model, the radial stress of the cavity surface can be obtained:

$$\sigma_r(\zeta = 0) = S(\zeta = 0)\tau_0 = A\tau_0 + B\rho_0 V^2, \quad (1)$$

$$A = \frac{1}{\alpha} \left(\frac{1 + \tau_0/2E}{\gamma} \right)^{2\alpha} - \frac{1}{\lambda},$$

$$B = \frac{3}{(1 - \eta^*)(1 - 2\alpha)(2 - \alpha)}$$

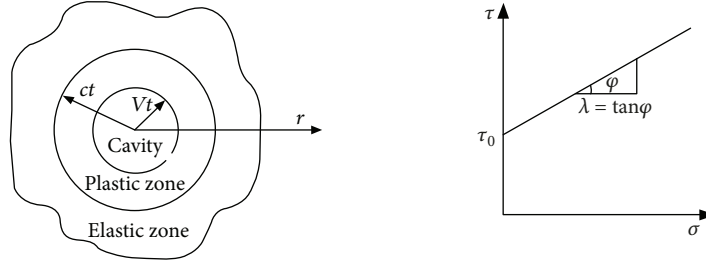
$$+ \frac{1}{\gamma^2} \left(\frac{1 + \tau_0/2E}{\gamma} \right)^{2\alpha} \left\{ \frac{3\tau_0}{E} + \eta^* \left(1 - \frac{3\tau_0}{2E} \right)^2 \right.$$

$$\left. - \frac{\gamma^3 [2(1 - \eta^*)(2 - \alpha) + 3\gamma^3]}{(1 - \eta^*)(1 - 2\alpha)(2 - \alpha)(1 + \tau_0/2E)^4} \right\}, \quad (2)$$

where $\alpha = 3\lambda/3 + 2\lambda$ ($\lambda = \tan \varphi$, where φ is the internal friction angle), $\eta^* = 1 - (\rho_0/\rho^*)$ (ρ_0 is the volume density before distortion and ρ^* is the volume density after distortion), $\gamma = V/c = [(1 + \tau_0/2E) - (1 - \eta^*)]^{1/3}$, E is Young model, and τ_0 is the cohesion of the medium.

3.1. Penetrating Force Analysis. When penetrating, the force on any shape of the anchor tip can be expressed as shown in Figure 9. Ignoring the force on the anchor body, the curve equation of the anchor tip is set as

$$r = f(z), 0 \leq z \leq p \text{ or } z = \varphi(r), \quad 0 \leq r \leq R. \quad (3)$$



(a) Schematic diagram of spherical cavity expansion model (b) Constitutive relation of medium

FIGURE 8: Schematic diagram of spherical cavity expansion model and constitutive relation of medium.

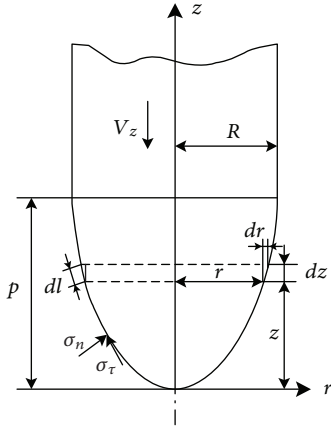


FIGURE 9: Force on the anchor tip with arbitrary shape.

As shown in equation (1), we can get

$$\sigma_n = A\tau_0 + B\rho_0 V_n^2, \quad (4)$$

where

$$\begin{aligned} V_n &= V_z \frac{dr}{dl} = V_z \cdot \frac{1}{\sqrt{1 + [\varphi'(r)]^2}} \\ &= V_z \cdot \frac{f'(z)}{\sqrt{1 + [f'(z)]^2}}. \end{aligned} \quad (5)$$

Force element on the anchor tip is

$$\begin{aligned} dF_n &= 2\pi r \sigma_n \sqrt{dz^2 + dr^2} = 2\pi r \sigma_n dl, \\ dF_\tau &= \mu dF_n = 2\pi r \mu \sigma_n dl. \end{aligned} \quad (6)$$

This force element on the axis direction is

$$dF_z = dF_n \frac{dr}{dl} + dF_\tau \frac{dz}{dl} = 2\pi r \sigma_n dr + 2\pi r \mu \sigma_n dz. \quad (7)$$

Thus, the axial force on the anchor tip is

$$\begin{aligned} F_{z1} &= 2\pi \int_0^r r \sigma_n dr + 2\pi \mu \int_0^z r \sigma_n dz, \quad 0 \leq z \leq p, \\ F_{z1} &= 2\pi \int_0^r r \sigma_n dr + 2\pi \mu \int_0^z r \sigma_n dz, \quad 0 \leq z \leq p. \end{aligned} \quad (8)$$

Substituting equation $\sigma_n = A\tau_0 + B\rho_0 V_n^2$ to equation (8), it can be obtained that

$$\begin{aligned} F_{z1} &= 2\pi \int_0^r \left(A\tau_0 + B\rho_0 V_z^2 \frac{1}{1 + [\varphi'(r)]^2} \right) r dr \\ &\quad + 2\pi \mu \int_0^z \left(A\tau_0 + B\rho_0 V_z^2 \frac{[f'(z)]^2}{1 + [f'(z)]^2} \right) \\ &\quad \cdot f(z) dz, \quad 0 \leq z \leq p, \end{aligned} \quad (9)$$

$$\begin{aligned} F_{z2} &= 2\pi \int_0^R \left(A\tau_0 + B\rho_0 V_z^2 \frac{1}{1 + [\varphi'(r)]^2} \right) r dr \\ &\quad + 2\pi \mu \int_0^p \left(A\tau_0 + B\rho_0 V_z^2 \frac{[f'(z)]^2}{1 + [f'(z)]^2} \right) \\ &\quad \cdot f(z) dz, \quad z > p. \end{aligned}$$

3.2. Penetrating Capability Analysis of the Typical Anchor Tip. Penetrating resistance analysis in Section 3.1 is universally available for arbitrary shape anchor tip. However, some anchor tip shape curves are complicated, which leads to the difficulty in getting the penetrating resistance value. Therefore, some typical shape anchor tips are analyzed. Typical shapes of anchor tips are shown in Figure 10, including flat head, round head, conic head, and ogival head. It is assumed that the anchor tips are rigid and do not deform during penetrating process.

(1) Flat anchor tip: it can be regarded as a cylindrical stick without anchor tip, and its penetrating force is

$$F_z = \pi R^2 (A\tau_0 + B\rho_0 V_z^2). \quad (10)$$

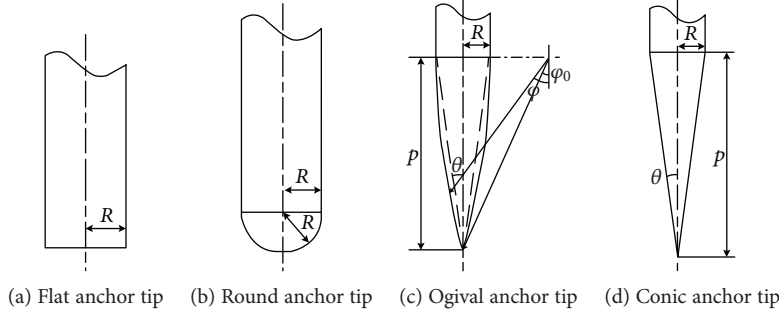


FIGURE 10: Schematic diagram of four typical anchor tips.

(2) Round anchor tip: generatrix equation of the round anchor tip is

$$R^2 = r^2 + (R - z)^2, \quad (11)$$

obtaining

$$\begin{cases} r = f(z) = \sqrt{R^2 - (R - z)^2}, \\ z = \varphi(r) = R - \sqrt{R^2 - r^2}, \end{cases} \quad (12)$$

thus,

$$\begin{cases} f'(z) = \frac{z - R}{\sqrt{R^2 - (R - z)^2}}, \\ \varphi'(r) = \frac{r}{\sqrt{R^2 - r^2}}. \end{cases} \quad (13)$$

Substituting the above equation to equation (9), it can be obtained that

$$\begin{aligned} F_{z1} &= 2\pi \int_0^r \left(A\tau_0 + B\rho_0 V_z^2 \cdot \frac{R^2 - r^2}{R^2} \right) r dr \\ &\quad + 2\pi\mu \int_0^z \left(A\tau_0 + B\rho_0 V_z^2 \cdot \frac{(z - R)^2}{R^2} \right) \\ &\quad \cdot \sqrt{R^2 - (R - z)^2} dz, \quad 0 \leq z \leq p, \\ F_{z2} &= 2\pi \int_0^R \left(A\tau_0 + B\rho_0 V_z^2 \cdot \frac{R^2 - r^2}{R^2} \right) r dr \\ &\quad + 2\pi\mu \int_0^p \left(A\tau_0 + B\rho_0 V_z^2 \cdot \frac{(z - R)^2}{R^2} \right) \\ &\quad \cdot \sqrt{R^2 - (R - z)^2} dz, \quad z > p, \end{aligned} \quad (14)$$

simplified as

$$\begin{aligned} F_{z1} &= \pi A\tau_0 r^2 + \pi B\rho_0 V_z^2 \left(r^2 - \frac{r^4}{2R^2} \right) \\ &\quad + 2\pi\mu \int_0^z \left(A\tau_0 + B\rho_0 V_z^2 \cdot \frac{(z - R)^2}{R^2} \right) \\ &\quad \cdot \sqrt{R^2 - (R - z)^2} dz, \quad 0 \leq z \leq p, \\ F_{z2} &= \pi R^2 \left(A\tau_0 + \frac{1}{2} B\rho_0 V_z^2 \right) \\ &\quad + 2\pi\mu \int_0^p \left(A\tau_0 + B\rho_0 V_z^2 \cdot \frac{(z - R)^2}{R^2} \right) \\ &\quad \cdot \sqrt{R^2 - (R - z)^2} dz, \quad z > p. \end{aligned} \quad (15)$$

(3) Ogival anchor tip: generatrix equation of the ogival anchor tip is

$$[r - (R - s)]^2 + (z - p)^2 = s^2 \quad 0 \leq z \leq p, 0 \leq r \leq R, \quad (16)$$

obtaining

$$\begin{cases} r = f(z) = \sqrt{s^2 - (z - p)^2} + (R - s), \\ z = \varphi(r) = \sqrt{s^2 - [r - (R - s)]^2} + p, \end{cases} \quad (17)$$

thus,

$$\begin{cases} f'(z) = \frac{p - z}{\sqrt{s^2 - (z - p)^2}} = \cot \phi, \\ \varphi'(r) = \frac{R - s - r}{\sqrt{s^2 - [r - (R - s)]^2}} = \tan \phi, \end{cases} \quad \phi > 45^\circ \text{ (the shape is round or convex when } \phi \leq 45^\circ \text{).} \quad (18)$$

Substituting the above equation to equation (9), it can be obtained that

$$\begin{aligned}
 F_{z1} &= 2\pi \int_0^r (A\tau_0 + B\rho_0 V_z^2 \cdot \cos^2 \phi) r dr \\
 &\quad + 2\pi\mu \int_0^z (A\tau_0 + B\rho_0 V_z^2 \cdot \cos^2 \phi) \\
 &\quad \cdot \left[\sqrt{s^2 - (z-p)^2} + (R-s) \right] dz, \quad 0 \leq z \leq p, \\
 F_{z2} &= 2\pi \int_0^R (A\tau_0 + B\rho_0 V_z^2 \cdot \cos^2 \phi) r dr \\
 &\quad + 2\pi\mu \int_0^p (A\tau_0 + B\rho_0 V_z^2 \cdot \cos^2 \phi) \\
 &\quad \cdot \left[\sqrt{s^2 - (z-p)^2} + (R-s) \right] dz, \quad z > p,
 \end{aligned} \tag{19}$$

owing to

$$\begin{cases} s - R + r = s \sin \phi, \\ p - z = s \cos \phi, \end{cases} \tag{20}$$

thus,

$$\begin{cases} r = s \sin \phi + R - s, \\ z = p - s \cos \phi. \end{cases} \tag{21}$$

Transforming equation (19) with above variable substitution, it can be obtained that

$$\begin{aligned}
 F_{z1} &= 2\pi s^2 \int_{\phi_0}^{\phi} (\sin \phi - \sin \phi_0) (\cos \phi + \mu \sin \phi) \\
 &\quad \times (A\tau_0 + B\rho_0 V_z^2 \cdot \cos^2 \phi) d\phi \quad 0 \leq z \leq p, \\
 F_{z2} &= 2\pi s^2 \int_{\phi_0}^{\pi/2} (\sin \phi - \sin \phi_0) (\cos \phi + \mu \sin \phi) \\
 &\quad \times (A\tau_0 + B\rho_0 V_z^2 \cdot \cos^2 \phi) d\phi \quad z > p.
 \end{aligned} \tag{22}$$

(4) Conic anchor tip: generatrix equation of the conic anchor tip is

$$\frac{r}{z} = \frac{R}{p} = \tan \theta, \tag{23}$$

obtaining

$$\begin{cases} r = f(z) = z \tan \theta, \\ z = \varphi(r) = r \cot \theta, \end{cases} \tag{24}$$

thus,

$$\begin{cases} f'(z) = \tan \theta, \\ \varphi'(r) = \cot \theta. \end{cases} \tag{25}$$

Substituting the above equation to equation (9), it can be obtained that

$$\begin{aligned}
 F_{z1} &= 2\pi \int_0^r (A\tau_0 + B\rho_0 V_z^2 \cdot \sin^2 \theta) r dr \\
 &\quad + 2\pi\mu \int_0^z (A\tau_0 + B\rho_0 V_z^2 \cdot \sin^2 \theta) z \tan \theta dz, \quad 0 \leq z \leq p, \\
 F_{z2} &= 2\pi \int_0^R (A\tau_0 + B\rho_0 V_z^2 \cdot \sin^2 \theta) r dr \\
 &\quad + 2\pi\mu \int_0^p (A\tau_0 + B\rho_0 V_z^2 \cdot \sin^2 \theta) z \tan \theta dz, \quad z > p.
 \end{aligned} \tag{26}$$

simplified as

$$\begin{aligned}
 F_{z1} &= \pi r^2 (A\tau_0 + B\rho_0 V_z^2 \cdot \sin^2 \theta) \\
 &\quad + 2\pi\mu \int_0^z (A\tau_0 + B\rho_0 V_z^2 \cdot \sin^2 \theta) z \tan \theta dz, \quad 0 \leq z \leq p, \\
 F_{z2} &= \pi R^2 (A\tau_0 + B\rho_0 V_z^2 \cdot \sin^2 \theta) \\
 &\quad + 2\pi\mu \int_0^p (A\tau_0 + B\rho_0 V_z^2 \cdot \sin^2 \theta) z \tan \theta dz, \quad z > p.
 \end{aligned} \tag{27}$$

The friction force on the anchor tip takes a very small proportion in total resistance force, which can be ignored. Thus, the resistance force on the anchor tip can be expressed as follows after the anchor tip has totally penetrated in the medium.

(1) Flat anchor tip

$$F_{z2} = \pi R^2 (A\tau_0 + B\rho_0 V_z^2), \quad z > p. \tag{28}$$

(2) Round anchor tip

$$F_{z2} = \pi R^2 \left(A\tau_0 + \frac{1}{2} B\rho_0 V_z^2 \right), \quad z > p. \tag{29}$$

(3) Ogival anchor tip

$$\begin{aligned}
 F_{z2} &= 2\pi s^2 \int_{\phi_0}^{\pi/2} (\sin \phi - \sin \phi_0) \\
 &\quad \times (A\tau_0 + B\rho_0 V_z^2 \cdot \cos^2 \phi) \cos \phi d\phi, \quad z > p.
 \end{aligned} \tag{30}$$

It can be simplified as

$$F_{z2} = \pi R^2 \left(A\tau_0 + B\rho_0 V_z^2 \cdot \frac{8\psi - 1}{24\psi^2} \right), \quad z > p, \quad (31)$$

where ψ is the curvature radius of the anchor tip, and its value is defined as

$$\psi = \frac{s}{2R}. \quad (32)$$

For an ogival anchor tip, whereas

$$s^2 = (s - R)^2 + p^2. \quad (33)$$

Thus,

$$\psi = \frac{s}{2R} = \frac{R^2 + p^2}{4R^2} = \frac{\tan^2\theta + 1}{4 \tan^2\theta} = \frac{1}{4 \sin^2\theta}. \quad (34)$$

(4) Conic anchor tip

$$F_{z2} = \pi R^2 (A\tau_0 + B\rho_0 V_z^2 \cdot \sin^2\theta), \quad z > p. \quad (35)$$

In conclusion, axial resistance force on the above-mentioned anchor tips can be expressed as

$$F_z = \pi R^2 (A\tau_0 + NB\rho_0 V_z^2), \quad z > p, \quad (36)$$

where N is the anchor tip shape coefficient, and N is

$$N = \begin{cases} 1, & \text{flat anchor tip,} \\ \frac{1}{2}, & \text{round anchor tip,} \\ \frac{8\psi - 1}{24\psi^2} = \frac{4}{3} \sin^2\theta - \frac{2}{3} \sin^4\theta, & (\theta < 45^\circ), \text{ ogival anchor tip,} \\ \sin^2\theta, & \text{conic anchor tip,} \end{cases} \quad (37)$$

Thus, the resistance forces of different shape anchor tips can be compared by the N value. Figure 11 shows the relationship between N and θ of four typical anchor tips. The smaller N is, the smaller the resistance force is. It can be seen that the penetrating resistance of the conic anchor tip is the smallest when $\theta \leq 45^\circ$, and the penetrating resistance of the round anchor is the smallest when $\theta \geq 45^\circ$. At the same time, it can be seen that the smaller θ is, the smaller the axial resistance is. Thus, the anchor tip of the anchoring system is designed to be conic.

3.3. Dimension Design of the Anchor Tip. For the conic anchor tip, its nominal curvature radius is

$$\psi' = \frac{p}{2R}. \quad (38)$$

Its shape coefficient is

$$N_z = \frac{1}{4\psi'^2 + 1}. \quad (39)$$

The relationship between N_z and ψ' of the conic anchor tip is shown in Figure 11, and it can be seen that N_z decreases exponentially with the increase of ψ' . The larger ψ' is, the smaller N_z is, and the smaller the resistance force is when penetrating. The smaller N_z represents the smaller sharp

angle θ of the conic anchor tip. However, too small sharp angle θ induces a more slender anchor tip, and this conic anchor tip is easy to be deformed in penetrating. Therefore, ψ' should not be too large. It can be seen from Figure 12 that the changing of N_z with ψ' is very slow when $\psi' \geq 3$. Thus, ψ' is selected to be 3 in designing the conic anchor tip.

When $\psi' = 3$,

$$\psi' = \frac{p}{2R} = 3. \quad (40)$$

It can be seen that the conic angle of the cone angle is

$$\theta = \arctan \frac{R}{p} \approx 9.46^\circ. \quad (41)$$

Taking the anchor tip diameter is 20 mm and the anchor tip length is 60 mm, because the half-apex angle of the conic anchor tip is 9.46° (the apex angle is 18.9°), we can get the shape of the conic anchor tip as shown in Figure 13(a). As the conic anchor tip is prone to bend during penetration, the conic anchor tip is evolved into the shape shown in Figure 13(b), and its tip is a cylinder with the diameter of 3 mm. This design ensures that the overall shape of the anchor tip is conic and conforms to the above dimensions and avoids the occurrence of bending damage at the top of the conic anchor tip. The tip is designed to be a cylinder with a diameter of 3 mm just considering simple machining. The

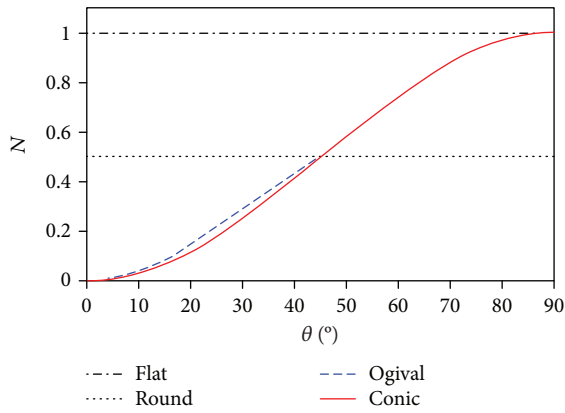


FIGURE 11: Relationship between N and θ of four typical anchor tips.

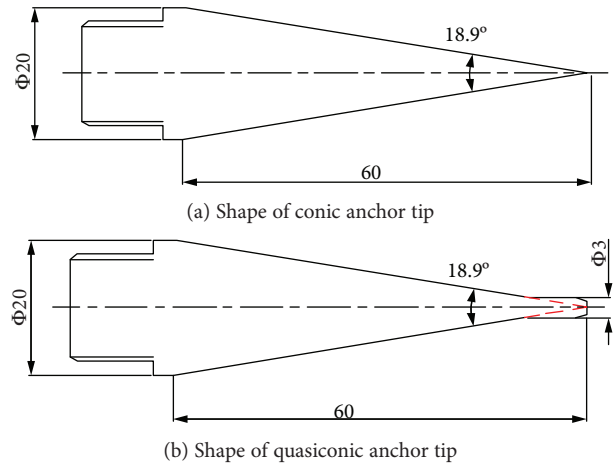


FIGURE 13: Schematic diagram of the conical anchor tip.

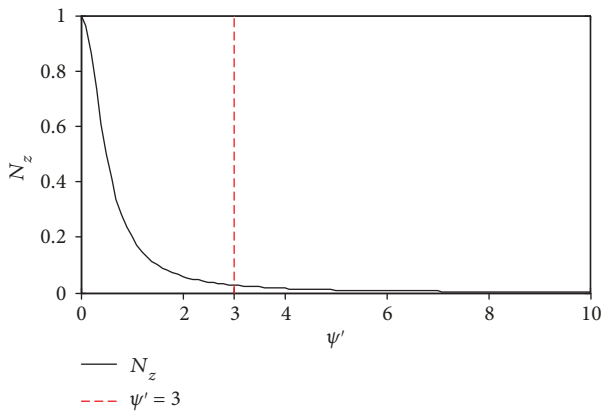


FIGURE 12: Relationship between N_z and ψ' of the conical anchor tip.

top of the anchor tip can also be designed to be other shapes such as sphere or something else, but it should not too large to affect the overall shape of the conical anchor tip.

3.4. Penetrating Ability Test of the Typical Anchor Tips. In order to verify the penetrating ability of several kinds of anchor tips mentioned above, different shapes of anchor tips such as flat, round head, ogival, conic, and quasiconic are manufactured, respectively, as shown in Figure 14. They are penetrated in the same clay medium. Due to the different mass of different anchor tips, the penetrating ability is analyzed by the relationship between the initial kinetic energy and the penetrating depth. The experimental results are shown in Figure 15. It can be seen from Figure 14 that under the same initial energy condition, the penetrating depth of the quasiconic, conic, and ogival anchor tips is close to each other, which can be seen as the deepest. The penetrating depth of the flat anchor tip is the shallowest, and the penetrating depth of the round anchor tip is deeper than that of the flat anchor tip. The experimental results are consistent with the above analysis results, and it also can be proved that the evolution of the conic anchor tip into the quasiconic anchor tip has little effect on its penetrating ability.



FIGURE 14: Several anchor tips with different shapes.

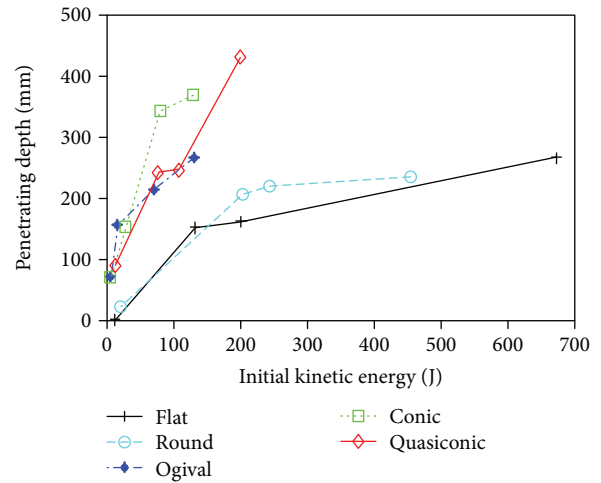


FIGURE 15: Penetrating capability of anchor tips with different shape.

4. Test of the Anchoring System

In order to verify the performance of the anchoring system, it is necessary to test the penetrating and anchoring capability of the anchoring system in a variety of different media.

4.1. Snow Medium. The density of the snow is about $100 \text{ kg/m}^3 \sim 400 \text{ kg/m}^3$, the corresponding shear strength is about $0.5 \text{ kPa} \sim 150 \text{ kPa}$ [17], and its shear strength is very

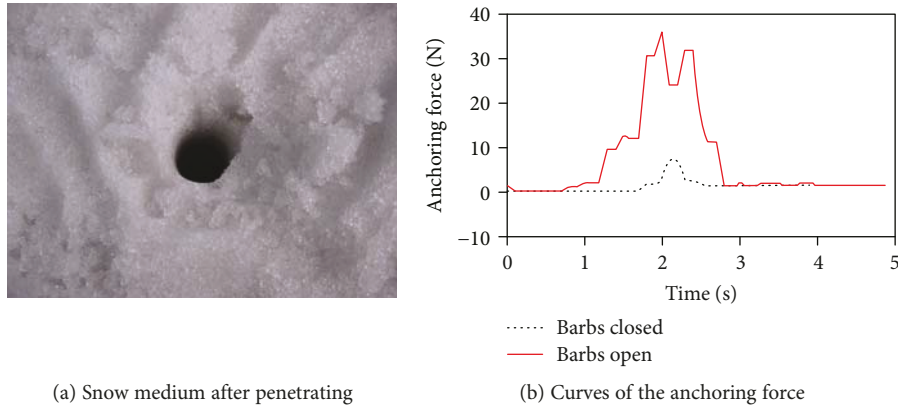


FIGURE 16: Penetrating and anchoring tests in snow medium.

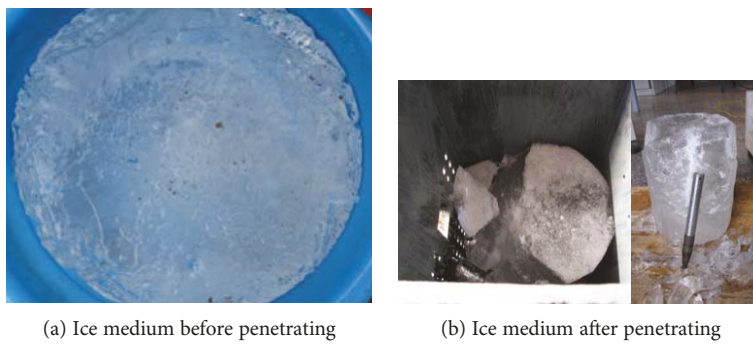


FIGURE 17: Penetration and anchoring tests in ice medium.

TABLE 2: Penetrating and anchoring tests in gypsum medium.

Test	1	2	3	4
Penetrating velocity	50.9 m/s	31.0 m/s	100.5 m/s	76.1 m/s
Penetrating result	Penetrated	Penetrated	Cracking	Crazing
Penetrating depth	65 mm	35 mm	---	125 mm
Anchoring force	107 N	---	---	25 N
Testing pictures				

low. When testing, the anchor body disappears in the snow and forms a hole with the diameter of the anchor body, as shown in Figure 16(a). The anchoring force is measured as shown in Figure 16(b). When the barb on the anchor body is not open, the maximum anchoring force is about 7.0 N. However, in the same case of penetration, when the barb on the anchor body is open, the maximum anchoring force is about 36.0 N. It shows that the barbs have obvious effect on enhancing the anchoring force.

4.2. *Ice Medium.* The shear strength of ice is about 0.7 MPa~3.1 MPa, and the average shear strength is about 1.43 MPa in the range of $-10^{\circ}\text{C} \sim -20^{\circ}\text{C}$ [17]. The penetrating speeds were 11.5 m/s and 25.1 m/s, and the ice cubes were completely broken, as shown in Figure 17. Since the ice was

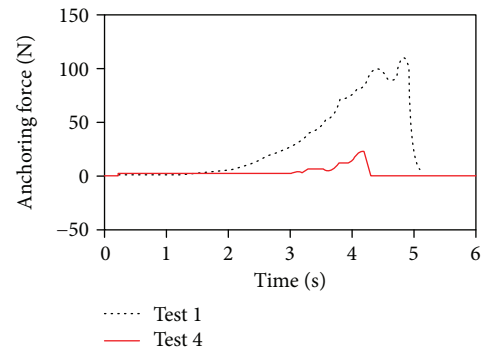


FIGURE 18: Anchoring force curves of the anchor body in gypsum medium.

TABLE 3: Penetrating and anchoring tests in cement.

Test	1	2	3	4
Compressive strength	7.1 MPa	9.7 MPa	9.7 MPa	13.3 MPa
Penetrating velocity	32.3 m/s	36.6 m/s	48.0 m/s	45.4 m/s
Penetrating result	Cracking	Penetrated	Cracking	Cracking
Penetrating depth	47 mm	10 mm	45 mm	30 mm
Anchoring force	---	80 N	---	---
Testing pictures				

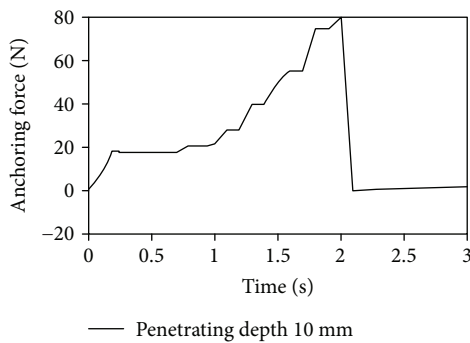


FIGURE 19: Anchoring force when anchor body penetrating 10 mm in 9.7 MPa cement medium.

broken in the tests, the anchorage was not performed. The experiment proves that the anchoring system can penetrate the ice medium.

4.3. *Gypsum Medium.* Gypsum medium is a brittle material. Its strength is higher than clay, but lower than cement. Tests are carried out on different velocities, and the corresponding anchoring forces are tested. The experimental results are shown in Table 2. The anchoring force curves of test 1 and test 4 are shown in Figure 18. It can be seen that the greater the penetrating velocity is, the greater the penetrating depth is. The greater speed induces gypsum cracking, while the gypsum cracking caused the decline of the anchoring force.

4.4. *Cement Medium.* Three kinds of cement with different compressive strength were used in the experiments. The parameters of the cement and the corresponding experimental results are shown in Table 3. It can be seen that the anchoring system can penetrate different strength cement media, and the cement is cracked by high-speed anchor body. The anchoring force curve in undamaged 9.7 MPa cement medium is shown in Figure 19, and its anchoring force is about 80 N.

4.5. *Ground Soil Geology.* In this experiment, the anchoring system was driven by pyrotechnics, and the experiment was carried out in the outdoor natural geology. The advancing unit of the anchor system is installed inside the protective cover, and the camera and light are set inside. The

experimental results are shown in Figure 20 and Table 4. In test 1, the soil is soft and its shear strength is small; thus, the anchor body is easy to penetrate but not easily anchored. Its anchoring force is only 60 N. In test 2, the shear strength of the soil is slightly larger than that in test 1; thus, the penetrating depth is smaller but the anchoring force is larger, and its anchoring force is 178 N.

By the way, by use of pyrotechnic driving, it shows that the anchoring system can be driven by the pyrotechnic system, and it is proved that the anchoring system of the asteroid landing mechanism is reasonable.

Experiments in different media verified that the anchoring system designed in the paper is reasonable. In the same medium, the higher the penetrating velocity is, the larger the penetrating depth and the anchoring force is. However, in some soft medium, high penetrating velocity will result in a large penetrating depth which may be larger than 2 m. This is easy to destroy the rope connecting between the penetrating unit and the winding unit. Thus, the penetrating velocity is not the higher the better. According to the experiment results, it can be found that the penetrating velocity in snow medium should be small, and the suggested velocity is ≤ 5 m/s; the penetrating velocity in petrous media such as ice, gypsum, cement, or ground soil should be as high as possible, and the suggested velocity is ≥ 30 m/s. However, high penetrating velocity needs high energy which will bring severe impact on the landing mechanism; thus, the suggested velocity is 30 m/s~100 m/s.

4.6. *Barbs' Effect on the Anchoring Force.* The anchor tip of the anchoring system is designed as a transformable structure in order to reduce the penetrating resistance and enhance the anchoring force. Before penetrating, the anchor tip is quasi-conic, and the barbs are embedded in the anchor tip. After penetrating, the barbs are opened and they enhanced the contact area between the anchoring system and the medium. In order to analyze the effect of the barbs on the anchoring performance, the anchoring forces of the anchor body with and without barbs with the same penetrating depth in the soft clay and the sand were experimentally measured. The experimental results are shown in Figure 21.

Figure 21(a) shows the anchoring force curves of two different anchor bodies in the same soft clay medium with

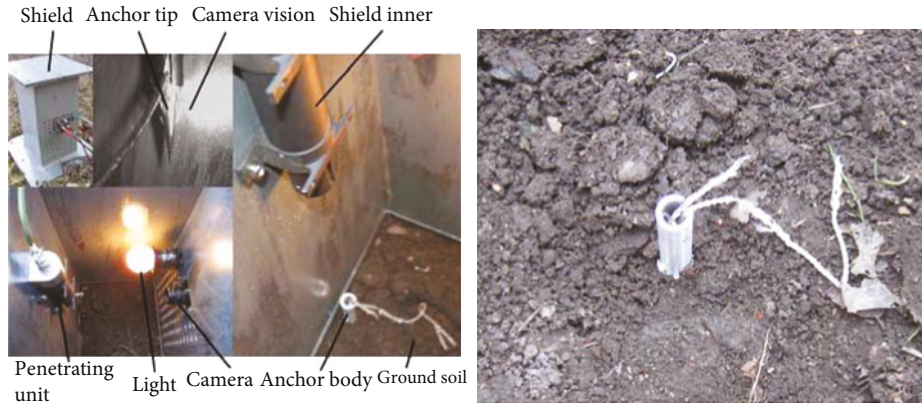


FIGURE 20: Test in ground soil geology.

TABLE 4: Testing results of anchoring system in ground medium.

	Test 1	Test 2
Pyrotechnical type	HgQB-8B (30 MPa/5 ml)	HgQB-8B (30 MPa/5 ml)
Penetrating velocity	About 50 m/s	About 50 m/s
Ground medium characteristics	There is frozen soil, and its shear strength is about 0.5 MPa.	The frozen soil is close-grained, and its shear strength is about 1~2 MPa.
Anchoring force	60 N	178 N

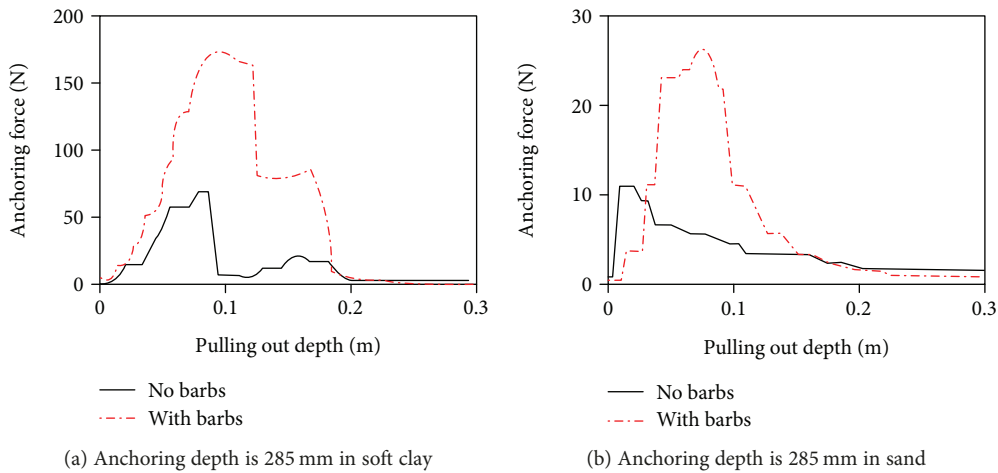


FIGURE 21: Anchoring force of anchor body with and without barbs.

285 mm penetrating depth. The maximum anchoring force of the anchor body with no barb is about 65 N, and the maximum anchoring force of the anchor body with barbs is about 170 N. The anchoring force is nearly tripled; Figure 21(b) shows the anchoring force curves of two different anchor bodies in the same sand medium with 285 mm penetrating depth. The maximum anchoring force of the anchor body with no barb is about 11 N, and the maximum anchoring force of the anchor body with barbs is about 25 N. The anchoring force is almost doubled. It is visible that the barbs have an important effect on increasing the anchoring force. At the same time, it can be seen that the effect of the barbs on the anchoring force is more obvious in hard medium than

that in soft medium. That is to say, the barbs play an important role in improving the anchoring performance.

5. Conclusions

In the paper, an anchoring system for the landing mechanism to the soft asteroid is designed. It is composed by penetrating unit, advancing unit, winding unit, and damping unit. The penetrating resistance of the anchoring system is greatly related to the shape of the anchor tip, and its shape is designed to be quasiconic. Deformable barbs adhibit on the surface of the anchor tip. Deformable barbs can greatly enhance anchoring force without increasing penetrating

resistance simultaneously. The penetrating and the anchoring performances of the anchoring system are validated in several media. Shear strength of these media has wide range, covering the demanded range 100 KPa~5 MPa. The maximum anchoring force of the anchoring system in snow, gypsum, cement, and ground soil medium is, respectively, 36 N, 107 N, 80 N, and 178 N, among which the latter three are larger than demanded value, namely 50 N. In conclusion, the anchoring system designed in the paper has reasonable penetrating and anchoring performance.

Data Availability

The data used to support the findings of this study are available from the corresponding author upon request.

Conflicts of Interest

The authors declare that they have no conflicts of interest.

Acknowledgments

This work is financially supported by the National High Technology Research and Development Program of China (863 Program) (no. 2008AA12A214) and the National Natural Science Foundation of China (no. 51105091, no. 51505028, and no.51775129).

References

- [1] R. P. Binzel, D. F. Lupishko, M. D. Martino, R. J. Whiteley, and G. J. Hahn, "Physical properties of near-earth objects," *Asteroids III*, vol. 255, no. 271, 2002.
- [2] B. R. Blair, "The role of near-earth asteroids in long-term platinum supply," *Space Resources Roundtable II*, pp. 1–15, 2000.
- [3] W. Xu and Z. Haibin, "Deep space exploration of asteroids," *The Science Perspectives*, vol. 20, no. 11, pp. 1183–1190, 2005.
- [4] M. D. Rayman and R. A. Mase, "Dawn's exploration of Vesta," *Acta Astronautica*, vol. 94, no. 1, pp. 159–167, 2014.
- [5] H. Yano, T. Kubota, H. Miyamoto et al., "Touchdown of the Hayabusa spacecraft at the Muses Sea on Itokawa," *Science*, vol. 312, no. 5778, pp. 1350–1353, 2006.
- [6] E. Asphaug, "Adventures in near-earth object exploration," *Science*, vol. 312, no. 5778, pp. 1328–1329, 2006.
- [7] S. R. Chesley, D. Farnocchia, M. C. Nolan et al., "Orbit and bulk density of the OSIRIS-REx target asteroid (101955) Bennu," *Icarus*, vol. 235, pp. 5–22, 2014.
- [8] J. Biele and S. Ulamec, "Capabilities of Philae, the Rosetta Lander," *Space Science Reviews*, vol. 138, no. 1–4, pp. 275–289, 2008.
- [9] S. Ulamec, C. Fantinati, M. Maibaum et al., "Rosetta lander-landing and operations on comet 67P/Churyumov-Gerasimenko," *Acta Astronautica*, vol. 125, pp. 80–91, 2016.
- [10] E. Gibney, "Mission accomplished: Rosetta crashes into comet," *Nature*, vol. 538, no. 7623, pp. 13–14, 2016.
- [11] J. P. Bibring, H. Rosenbauer, H. Boehnhardt et al., "The Rosetta Lander ("Philae") investigations," *Space Science Reviews*, vol. 128, no. 1–4, pp. 205–220, 2007.
- [12] A. D. Steltzner and A. K. Nasif, "Anchoring technology for in situ exploration of small bodies," in *2000 IEEE Aerospace Conference. Proceedings (Cat. No.00TH8484)*, pp. 507–518, Big Sky, Montana, USA, 2000.
- [13] Z. Zhao, J. Zhao, and H. Liu, "Development of a landing mechanism for asteroids with soft surface," *International Journal of Aerospace Engineering*, vol. 2013, Article ID 873135, 9 pages, 2013.
- [14] X. Jianbo, *Investigations on long projectiles penetrating into concrete targets*, National University of defense Technology, 2001.
- [15] T. He, *A Study on the Penetration of Projectiles into Targets Made of Various Materials*, University of Science and Technology of China, 2007.
- [16] M. J. Forrestal and V. K. Luk, "Penetration into soil targets," *International Journal of Impact Engineering*, vol. 12, no. 3, pp. 427–444, 1992.
- [17] J. J. Petrovic, "Review mechanical properties of ice and snow," *Journal of Materials Science*, vol. 38, no. 1, pp. 1–6, 2003.



Hindawi

Submit your manuscripts at
www.hindawi.com

